JOURNAL OF THERMOPHYSICS AND HEAT TRANSFER
Vol. 24, No. 1, January–March 2010

Mach Number, Reynolds Number, Jet Spacing Variations: Full Array of Impinging Jets

Matt Goodro* and Phil Ligrani†
Oxford University, Oxford, England OX2 6AQ, United Kingdom
and
Mike Fox‡ and Hee-Koo Moon§
Solar Turbines, Inc., San Diego, California 92186-5376

DOI: 10.2514/1.44029

Presented are data that illustrate the effects of Mach number, Reynolds number, and hole spacing on surface Nusselt numbers produced by an array of jets impinging on a flat plate. Considered are Reynolds numbers ranging from 17,300 to 60,000 and Mach numbers from 0.1 to 0.45. Impingement hole spacings are 5*D*, 8*D*, and 12*D* in the streamwise and spanwise directions. Local spatially resolved and spatially averaged Nusselt numbers, measured using infrared thermography and energy balance techniques, show strong dependence on the impingement jet Reynolds number for each situation as the jet Mach number is maintained constant. Nusselt numbers show negligible variations between $Ma = 0.1$ and 0.2; however, data taken at Mach numbers greater than 0.2 (as the Reynolds number is held constant) show that Mach number has a significant impact on local and spatially averaged Nusselt numbers. This Mach number dependence changes with hole spacing, with greater Nusselt number increases with the less dense impingement arrays. These variations are described using new correlations, which account for the effects of Mach number for all three impingement hole spacings.

Nomenclature

A	=	impingement hole area, m^2
A_{ht}	=	heat transfer area on the target plate, m^2
C_D	=	discharge coefficient
c_a	=	impingement airflow sonic velocity, m/s
D	=	diameter of an individual impingement hole, m
Gc	=	crossflow mass velocity, $kg/m^2 \cdot s$
Gj	=	jet mass velocity, $kg/m^2 \cdot s$
h_{loss}	=	heat transfer coefficient to account for convection and radiation loss on back side of target plate, $W/m^2 \cdot K$
k	=	ratio of specific heats
M_a	=	impingement airflow Mach number
M_i	=	impingement airflow ideal Mach number
$\dot{m}$	=	impingement air mass flow rate, kg/s
Nu	=	local Nusselt number
$\overline{Nu}$	=	line-averaged Nusselt number
$\overline{\overline{Nu}}$	=	spatially averaged Nusselt number
P_a	=	impingement air static pressure, Pa
P_{oj}	=	impingement air stagnation pressure, Pa
Q	=	total power provided to the thermofoil heater, W
q_{cb}	=	convection heat flux from back side of the target plate, W/m^2
q_{cf}	=	convection heat flux from front side (or impingement side) of the target plate, W/m^2
q_{rb}	=	radiation heat flux from back side of the target plate, W/m^2
q_{rf}	=	radiation heat flux from front side (or impingement side) of the target plate, W/m^2
R	=	ideal gas constant
Re_j	=	impingement airflow Reynolds number
$T_{ambient}$	=	ambient static temperature, K
T_b	=	local temperature on the back surface of the polystyrene target plate, K
Ti	=	impingement air ideal static temperature, K
T_j	=	impingement air static temperature, K
T_{oj}	=	impingement air stagnation temperature, K
T_{tc}	=	local thermocouple temperature between the heater and the polystyrene target plate, K
T_W	=	local target surface temperature on the surface of the heater adjacent to impingement air, K
u_a	=	impingement air velocity, m/s
$u_{crossflow}$	=	crossflow air velocity, m/s
u_i	=	impingement air ideal velocity, m/s
u_{jet}	=	jet air velocity, m/s
X	=	streamwise distance between centerlines of adjacent impingement holes, m
x	=	streamwise coordinate, m
Y	=	spanwise distance between centerlines of adjacent impingement holes, m
y	=	spanwise coordinate, m
Z	=	distance between target plate and impingement hole plate, m
z	=	normal coordinate, m
α	=	air thermal conductivity, $W/m \cdot K$
ε_f	=	emissivity of the front surface of the target plate
ε_{inf}	=	emissivity of a plate located opposite to the target plate
μ	=	absolute viscosity, $kg/m \cdot s$
ρ_a	=	impingement air static density, kg/m^3
ρ_i	=	impingement air ideal static density, kg/m^3
σ	=	Boltzman constant

I. Introduction

IMPINGEMENT cooling is an attractive method heat transfer augmentation because its effectiveness is relatively high, making it a viable tool for heat load management. The main objective of such

Received 25 February 2009; revision received 30 August 2009; accepted for publication 14 October 2009.

*Ph.D. Graduate Student, Department of Engineering Science; currently Research Engineer, Neurobehavioral Research, Inc., Honolulu, Hawaii 96814.

†Donald Schultz Professor of Turbomachinery, Department of Engineering Science; currently 1401 Blumberg Boulevard, Number 400, Winter Springs, Florida 32708; p_ligrani@msn.com (Corresponding Author).

‡Consulting Engineer, Aero/Thermal & Heat Transfer, 2200 Pacific Highway, Post Office Box 85376, Mail Zone C-9.

§Heat Transfer Manager, Aero/Thermal & Heat Transfer, 2200 Pacific Highway, Post Office Box 85376, Mail Zone C-9.

cooling is maximum heat removal with minimal coolant mass flow rates. As such, impingement cooling is used for a variety of applications, including cooling the insides of high external heat load regions, such as the stagnation region, within turbine components of gas turbine engines [1]. Impingement cooling is also often used to cool parts of the combustor in gas turbine engines, including combustion chamber liners, transition pieces, and splash plates [2].

Most existing impingement investigations consider the effects of changing impingement plate geometric and configuration parameters, and physical parameters in flows with low Mach numbers, and relatively low speeds. Of these studies, Kercher and Tabakoff [3] showed that spatially averaged heat transfer coefficients are dominated by the Reynolds number, and streamwise/spanwise hole spacing. These investigators present spatially averaged surface heat transfer coefficients beneath an array of impinging jets in low-speed flow for Reynolds numbers from 3×10^2 to 3×10^4, X/D and Y/D from 3.1 to 12.5, and Z/D from 1.0 to 4.8. Metzger et al. [4] and Chupp et al. [5] considered heat transfer within airfoil leading-edge regions by measuring the heat transfer with a semicircular concave region with a line of circular jets impinging on the apex, considering the effects of target spacing, hole spacing, and jet Reynolds number. Metzger and Korstad [6] examined the influences of crossflow on a single line of jets, emerging from circular holes, placed on one wall of a channel. Chance [7] investigated low-speed impingement cooling with spent air constrained to flow out of only one side of the flow passage. He presents data at Reynolds numbers from 6×10^3 to 5×10^4; square, equilateral triangle, and rectangular jet arrays; Z/d values of 2, 3, 4, 6, and 8; and ratios of impingement to surface absolute temperature of 0.77, 1.27, and 1.54. In another paper, Metzger et al. [8] indicated that in-line jet impingement hole patterns provide better heat transfer than staggered arrangements. Investigated are Z/D values of 1, 2, and 3; X/D and Y/D ranging from 6 to 32; and Reynolds numbers from 5×10^3 to 2×10^4. Florschuetz et al. [9] described a continuation of this investigation, wherein Reynolds numbers from 2.5×10^3 to 7×10^4, in-line and staggered hole patterns, Z/D from 1 to 3, X/D from 5 to 15, and Y/D from 4 to 8 are considered. Included are data on channel crossflow mass velocity and jet mass velocity (for which ratios range from 0 to 0.8), as well as a correlation that gives Nusselt number dependence on these parameters, as well as on jet impingement plate geometry, Prandtl number, and Reynolds number.

Obot and Trabold [10] considered different crossflow schemes on impingement heat transfer in low-speed flows. Impingement jet Reynolds numbers from 1×10^3 to 2.1×10^4, Z/D values from 2 to 16, X/D values of 5 and 10, and Y/D values of 4 and 8 are employed. Bunker and Metzger [11] presented detailed local heat transfer distributions due to line jet impingement for leading-edge regions, both with and without film extraction effects. Fox et al. [12] examined the effects of unsteady vortical structures on the adiabatic wall temperature distribution produced by a single impinging jet. Bailey and Bunker [13] investigated impingement arrays with in-line jets in a "square array," with axial and lateral jet spacings of 3, 6, and 9. Reynolds numbers ranged from 1.4×10^4 to 6.5×10^4, Mach numbers were relatively low, and jet plate-to-target spacings ranged from 1.25 to 5.5 impingement hole diameters.

Other recent studies consider the effects of jet impingement on a leading edge/concave wall with roughness [14], and the effects of jets with mist and steam on a concave target surface [15]. Parsons et al. [16,17], Parsons and Han [18], Epstein et al. [19], and Mattern and Hennecke [20] showed that rotational effects are important for jets impinging on flat surfaces at relatively low Reynolds numbers. In another recent investigation that employs flat target plates, Brevet et al. [21] considered the effects of impingement distance, Reynolds number, and spanwise hole spacing on Nusselt number distributions, which led to recommendations for optimal Z/D values of 2–5 and optimal spanwise hole spacings of 4–5 hole diameters. These investigators considered one row of impinging jets in a test section with low-speed flow in which the spent air was again constrained to exit in one direction. Brevet et al. [22] described recovery factors and Nusselt numbers measured on a flat target surface beneath a single, compressible impingement jet. Results are given for Z/D ratios from 2 to 10 and for Mach numbers from 0.02 to 0.69. Behbahani and Goldstein [23] gave correlation equations for local heat transfer due to staggered arrays of impinging circular air jets for two different jet-to-jet spacings, $4D$ and $8D$, and three different Reynolds numbers, 5000, 10,000, and 15,000. The investigations showed that area-averaged Nusselt numbers became smaller because the cooling area was smaller, when the jet-to-jet spacing was larger. San and Lai [24] investigated jet-to-jet spacing to optimize surface heat transfer for staggered arrays of impinging air jets. Downs and James [25], Jambunathan et al. [26], and Viskanta [27] presented reviews of several other jet impingement investigations.

The present study is aimed at providing new spatially resolved impingement heat transfer data that illustrate the effects of hole spacing at different Reynolds numbers and Mach numbers. As such, the data presented cover new experimental conditions that are not addressed in previous investigations [28]. In the present study, hole spacings of $5D$, $8D$, and $12D$ are employed. The thickness of each impingement plate is $1D$, and the spacing between the hole exit planes and the target plate is $3D$. Included are discharge coefficients, crossflow-to-jet mass velocity ratios, as well as local, line-averaged, and spatially averaged Nusselt numbers. In particular, data are presented for a constant Reynolds number, as the Mach number changes to values as high as 0.59. Data are also given that illustrate the separate dependences of local and spatially averaged Nusselt numbers on jet Mach number and jet Reynolds number for different hole jet spacings. Different hole spacings result in different interactions between adjacent jets, and between jets and wall boundary layers, which, when coupled with compressibility, give different local Nusselt number dependence on Mach number.

II. Experimental Apparatus and Procedures

The experimental apparatus and procedures that are employed are described by Goodro et al. [28]. Details of these items are also given here so that complete information are available to the reader.

A. Impingement Flow Facility and Impingement Plate

Schematic diagrams of the facility used for heat transfer measurements are presented in Figs. 1 and 2. The facility is constructed of 6.1-mm-thick American Society for Testing and Materials A38 steel plates, and A53 Grade B ARW steel piping. The airstream circulates in an open loop, as shown in Fig. 1. To achieve the Reynolds numbers of the present study, a Drum Industries 50 hp, D807 pressure blower is employed. The air mass flow rate provided to the test section is measured using an American Society of Mechanical Engineers (ASME) Standard orifice plate, flow-mounted chromel–alumel thermocouples, and HCX series fully signal conditioned pressure transducers (with diaphragms rated at 50 or 1000 mbar) connected to a National Instruments (NI) PCI-4351 high-precision temperature and voltage logger. The blower exits into a series of two plenums arranged in series; the upstream plenum is 0.63 m in length along each side, and the downstream plenum dimensions are 0.63, 0.77, and 0.77 m. A Bonneville crossflow heat exchanger is located within each plenum. As the air exits the heat exchanger, and the second plenum, the air passes into a 0.22 m outer diameter pipe, which contains the ASME Standard orifice plate

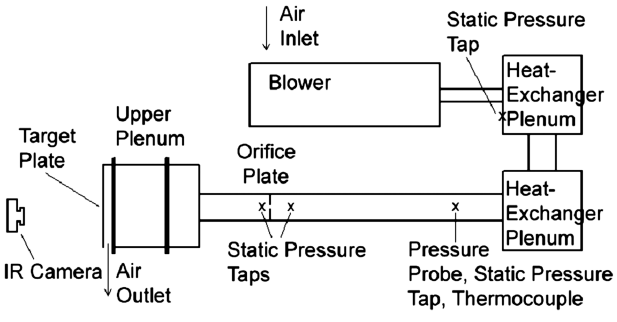

Fig. 1 Impingement flow facility.

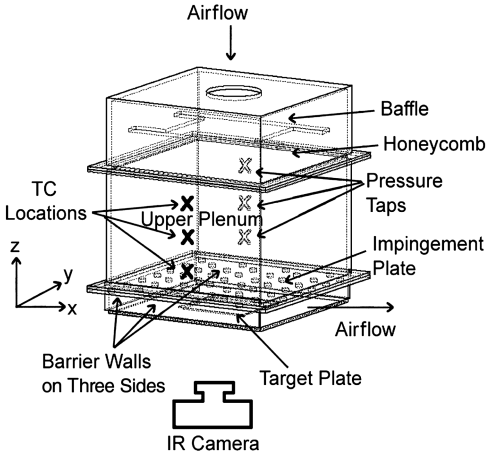

Fig. 2 Impingement flow facility test section, including impingement plenum and impingement channel.

employed to measure the air mass flow rate. This pipe then connects to the 0.63 m by 0.63 m side of the plenum shown in Fig. 2. Upon entering this plenum, the air first encounters a flow baffle used to distribute the flow, a honeycomb, and other flow straightening devices. These are followed by the impingement plenum (or upper plenum, located below the honeycomb and flow straightening devices in Fig. 2) with top dimensions of 0.635 m and 0.635 m and a height of 0.40 m.

Individual plates with holes used to produce the impingement jets are located at the bottom of this plenum, also shown in Fig. 2. The plenum is thus designed so that different impingement plates can be installed at this location. Figure 3 shows that each impingement plate is arranged with 10 rows of holes in the streamwise direction, arranged so that holes in adjacent rows are staggered with respect to each other. With this arrangement, either 9 or 10 holes are located in each streamwise row. The spacings between holes in the streamwise direction X are then $5D$, $8D$, or $12D$, and the spanwise spacings between holes in a given streamwise row Y are also $5D$, $8D$, or $12D$. The thickness of each impingement plate is $1D$. The spacing between the hole exit planes and the target plate is denoted Z and is equal to $3D$. Note that the coordinate system employed is also shown in Fig. 2. The impingement cooling flow that issues from these holes is contained within the channel formed by the impingement jet plate and the target surface, and is constrained to exit in a single direction, which is denoted here as the x direction. This channel is called the lower plenum. In the present study, the hole diameter size, D, blower, mass flow rate, and pressure level are employed so that the Mach number ranges from 0.1 to 0.45 and the Reynolds number is between 17,300 and 60,000. The impingement jet Mach number is varied as the impingement jet Reynolds number is held constant by conducting tests at different experimental conditions using impingement plates with different hole diameters, but with the same X/D and Y/D scaling. Similar procedures are employed to obtain experimental data as the impingement jet Reynolds number is varied with constant impingement jet Mach number.

B. Target Plate Test Surfaces for Measurements of Surface Nusselt Numbers

The polystyrene target plate is 1.58 mm thick and is mounted on the bottom surface of the plenum (as shown in Fig. 2) using gray cloth tape with PVC cement, a solvent containing methyl ethyl ketone, tetrahydrofuran, and acetone to seal the edges so that no leaks are present along the flow passage. A mounting frame is also employed to hold the solid polystyrene target plate in place, and to keep it smooth (without bending or wrinkles), and normal to the impingement jets, as testing is underway. Ten calibrated, chromel–alumel thermocouples are placed at different streamwise and spanwise locations within the polystyrene target plate so that each senses a different temperature as data are acquired. Each one of these thermocouples is mounted approximately 0.016 cm just below the surface adjacent to the air containing the impingement fluid. These provide measurements of local surface temperatures, after correction for thermal contact resistance and temperature drop through the 0.016 cm thickness of polystyrene. Thermocouple lead wires are placed in grooves along the polystyrene, and bonded into place with epoxy having approximately the same thermal conductivity as polystyrene, to minimize thermal disturbances resulting from their presence. Each one of these thermocouple wires is then located between the thermofoil heater and the polystyrene portion of the target plate.

Spatially resolved distributions of surface heat transfer coefficients and Nusselt numbers are measured on the polystyrene target plates with heaters and thermocouples attached. The custom-made HK5184R26 thermofoil heaters employed are manufactured by Minco Products, Inc., and have a temperature rating of 100°C. The etched-foil heating element within this device is encased between two layers of DuPont Kapton polyimide film. This heater is located adjacent to the airstream with the impinging air jets to provide a constant surface heat flux boundary condition adjacent to the impingement airstream. Its thermal conductivity is approximately 0.2 W/mK at 20°C. Polystyrene is chosen for the target plate because of its strength, and because it does not deform in shape at temperatures as high as 80°C. It is also suitable because of its relatively low thermal conductivity (0.09 W/mK at 20°C), which results in minimal streamwise and spanwise conduction along the test surface. The back side of this polystyrene plate is viewed by the infrared camera as spatially resolved measurements of surface temperature are obtained. Each polystyrene target plate is 1.27 mm thick and each heater is approximately 0.3 mm thick, giving a total target plate thickness of 1.58 mm. Because of the wear and degradation that results from exposure to different temperature levels as tests are conducted, including thermofoil heater wrinkling, these target plates are replaced with all new components after three or four individual test sequences.

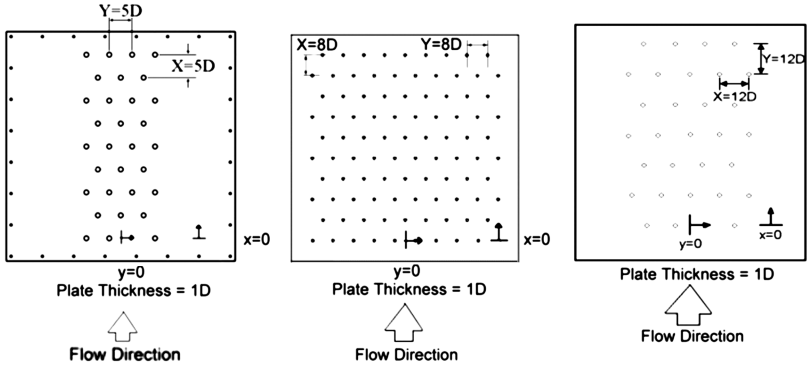

a) b) c)

Fig. 3 Impingement test plate configurations: a) $X/D = Y/D = 5$, b) $X/D = Y/D = 8$, and c) $X/D = Y/D = 12$.

C. Local Impingement Air Pressure and Temperature Measurements

As shown in Fig. 2, three wall static pressure taps are located on the surface of the upper plenum. Eight wall pressure taps are also located on the surface of the lower plenum for measurement of local static pressures. As tests are conducted, HCX series fully signal conditioned pressure transducers (with diaphragms rated at 50 or 1000 mbar) connected to an NI PCI-4351 high-precision temperature and voltage logger are used to sense pressures from these static pressure tappings. Local airflow recovery temperatures are measured using two calibrated chromel–alumel thermocouples located in the central part of the lower plenum, and three calibrated chromel–alumel thermocouples located in the central part of the upper plenum. In each case, readings from either multiple thermocouples or multiple pressure taps are used to obtain average values of measured quantities for a given plenum. Voltages from the pressure transducers and all thermocouples employed in the study are read sequentially using the NI PCI-4351 high-precision temperature and voltage logger. This system provides thermocouple compensation electronically such that voltages for type K chromel–alumel thermocouples are given relative to 0°C. The voltage outputs from this unit are acquired by the Dell Precision 530 PC workstation through the PCI card, using LABVIEW 7.0 software.

Because the overall volume and cross-sectional area of the upper plenum are large compared to the area of the impingement holes, the velocity and Mach number of the air in this plenum are both near zero. As a result, the static pressure measured at the wall static pressure taps is the same as the stagnation pressure, and is denoted P_{oj} (Pa), the impingement air stagnation pressure. The measured air recovery temperature in the upper plenum is then the same as the upper plenum static temperature and upper plenum stagnation temperature. This resulting value is denoted T_{oj} (°C), the impingement stagnation temperature. After measurement of the impingement air mass flow rate at the pipe orifice plate, the impingement air mass flux is determined using $\rho_a u_a = \dot{m}/A$.

An iterative procedure is then used to determine the impingement static temperature T_j (°C), and the impingement flow Mach number M_a. The first step in this procedure is estimation of the value of T_j (°C). The local recovery temperature, which is measured in the lower plenum, is used for this estimation. The impingement static density and spatially averaged impingement jet velocity are then determined using $\rho_a = P_a/RT_j$ and $u_a = \dot{m}/\rho_a A$, respectively. Because the impingement flow vents to the laboratory, the local atmospheric pressure is used for P_a (Pa). Measurements of lower plenum static pressures using wall pressure taps confirm this approach. Next, the impingement air sonic velocity and Mach number are given by $c_a = (kRT_j)^{1/2}$ and $M_a = u_a/c_a$, respectively. Iterations using these analysis steps are then continued until the impingement static temperature and impingement Mach number are consistent with the isentropic equation given by

$$T_j = T_{oj}/[1 + M_a^2(k-1)/2] \tag{1}$$

With impingement static temperature T_j (°C), impingement flow Mach number M_a, and other parameters known, the impingement Reynolds number is subsequently given by an equation of the form

$$Re_j = \rho_a u_a D/\mu \tag{2}$$

A Kiel-type stagnation pressure probe is used to measure the total pressure in the pipe at a position that is located upstream of the orifice plate employed to measure mass flow rate. A wall pressure tap located on the surface of the pipe and a calibrated chromel–alumel thermocouple positioned within the airstream are used to sense static pressure and flow recovery temperature, respectively, at the same streamwise location. Pressures and temperatures measured using the thermocouple, probe, and tap are sensed and processed using the same types of instrumentation mentioned earlier. The velocities deduced from this arrangement are used to provide a crosscheck on the velocities deduced from mass flow rates, which are measured using the ASME Standard orifice plate. The spatially averaged flow velocity from these two techniques are generally in agreement within ±3%.

D. Local Nusselt Number Measurement

The power to the thermofoil heater, mounted on the target plate, is controlled and regulated using a variac power supply. The total power supplied to the thermofoil heater is determined from measurements of the rms voltage and rms current, measured using a Hewlett–Packard digital voltmeter and an analog ammeter, respectively. Energy balances, and analysis to determine temperature values on the two surfaces of the target plate, then allow determination of the magnitude of the total convective power (due to impingement cooling) for a particular test. To determine the surface heat flux (used to calculate heat transfer coefficients and local Nusselt numbers), the total convective power level, provided by the particular thermofoil heater employed, is divided by the single surface area of this heater, denoted A_{ht} (m^2).

One step in this procedure uses a one-dimensional conduction analysis, which is applied between the surface *within* the target plate where the thermocouples are located (between the heater and the polystyrene target plate) and the ambient air environment behind the target plate. This is used to determine T_b (°C), the local temperature on the back surface of the polystyrene target plate, adjacent to the surrounding ambient air environment. Also required for this analysis is T_{tc} (°C), the local temperature within the target plate between the heater and the polystyrene plate, which is determined from thermocouple measurements. With these temperatures known, the radiation heat flux and the convection heat flux from the back side of the target plate, q_{rb} (W/m^2) and q_{cb} (W/m^2), respectively, are determined together using an equation of the form

$$q_{\text{rb}} + q_{\text{cb}} = h_{\text{loss}}(T_b - T_{\text{ambient}}) \tag{3}$$

where h_{loss} (W/m$^2 \cdot$ K) is assumed to be equal to 15 W/m$^2 \cdot$ K [21]. The radiation heat flux q_{rf} (W/m^2) on the front (or impingement side) of the target plate is determined using

$$q_{\text{rf}} = \sigma(1/\varepsilon_{\text{inf}} - 1/\varepsilon_f - 1)^{-1}(T_W^4 - T_{\text{ambient}}^4) \tag{4}$$

With this approach, the radiation heat flux is determined for an arrangement with multireflection between two infinite plates where each has a uniform temperature. ε_f and ε_{inf} are assumed to be equal to 0.9 for all conditions investigated. This approximate approach works well because $q_{\text{rf}}A_{\text{ht}}$ is generally only 3–6% of Q (W), the total amount of power provided to the thermofoil heater. Note that T_W (°C), the local target surface temperature on the surface of the heater adjacent impingement air, must be known to determine q_{rf} (W/m^2). Because of the interdependence of T_W (°C), q_{rf} (W/m^2), and q_{cf} (W/m^2) (the convection heat flux from the front side or impingement side of the target plate), an iterative procedure is required to determine these quantities. The next part of this procedure uses a one-dimensional conduction model for the heater, which includes source generation of thermal energy, to provide a relation between T_W (°C),

Table 1 Impingement test plate configurations

Hole diameter, mm	Plate thickness, mm	Hole spacing, X, Y, mm
3.5	3.5	17.5
3.5	3.5	28
3.5	3.5	42
4.5	4.5	22.5
4.5	4.5	36
4.5	4.5	54
8	8	40
8	8	64
8	8	96
15	15	75
15	15	120
15	15	180

Table 2 Experimental conditions of the present investigation

Re_j	M_a	D, mm	X/D, Y/D
17,300	0.20	4.5	5
30,000	0.10	15	5
30,000	0.20	8	5
30,000	0.30	4.5	5
30,000	0.38	3.5	5
60,000	0.20	15	5
17,300	0.20	4.5	8
30,000	0.20	8	8
30,000	0.35	4.5	8
30,000	0.45	3.5	8
60,000	0.20	15	8
17,300	0.20	4.5	12
30,000	0.10	15	12
30,000	0.20	8	12
30,000	0.38	4.5	12
30,000	0.45	3.5	12
60,000	0.20	15	12

T_{tc} (°C), and q_{cf} (W/m^2). Also included in the analysis is thermal contact resistance between the internal thermocouples and the adjacent heater.

The convection heat flux from the front side (or impingement side) of the target plate is then given by

$$q_{cf} = Q/A_{ht} - q_{rf} - q_{rb} - q_{cb} \tag{5}$$

The local Nusselt number is then given as

$$Nu = q_{cf}D/((T_W - T_{oj})\alpha) \tag{6}$$

As impingement heat transfer measurements are made, spatially resolved distributions of the target test surface temperature T_W (°C) are determined using infrared imaging in conjunction with thermocouples, energy balances, digital image processing, and in situ calibration

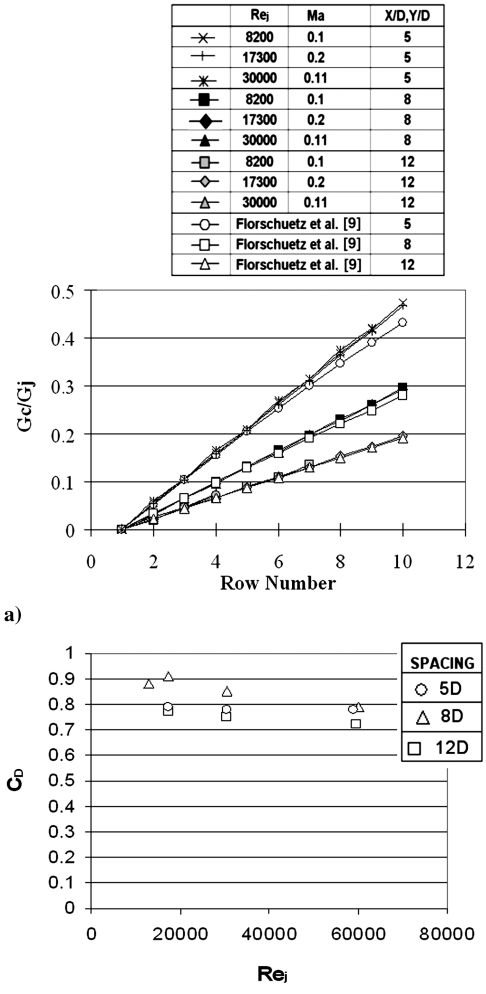

Fig. 4 Flow characteristics: a) Crossflow-to-jet mass velocity ratio with row number for hole spacings of 5*D*, 8*D*, and 12*D*; and b) discharge coefficient variations with Re_j for hole spacings of 5*D*, 8*D*, and 12*D* at a constant Mach number of 0.2.

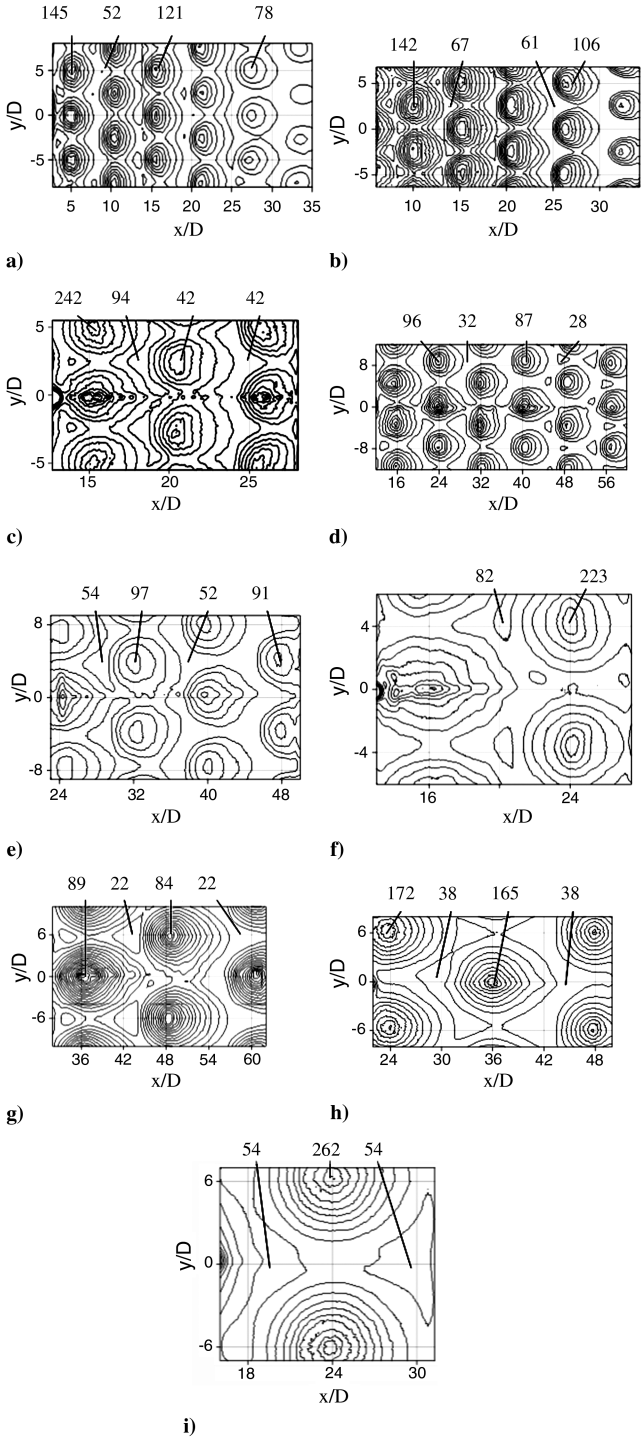

Fig. 5 Spatially resolved distributions of surface Nusselt number for $M_a = 0.2$ with hole spacings and Re_j values: a) 5*D* and $Re_j = 17,300$, b) 5*D* and $Re_j = 30,000$, c) 5*D* and $Re_j = 60,000$, d) 8*D* and $Re_j = 17,300$, e) 8*D* and $Re_j = 30,000$, f) 8*D* and $Re_j = 60,000$, g) 12*D* and $Re_j = 17,300$, h) 12*D* and $Re_j = 30,000$, and i) 12*D* and $Re_j = 60,000$.

procedures. These are then used to determine spatially resolved surface Nusselt numbers. To accomplish this, the infrared radiation emitted by the heated interior surface of the channel is captured using a FLIR Systems, Inc., ThermoVision® A20M Compact Temperature Measurement Infrared Camera (S/N 22700776), which operates at infrared wavelengths from 7.5 to 13.0 μm. Temperatures, measured using the calibrated, chromel–alumel thermocouples distributed along the test surface adjacent to the flow, are used to perform the in situ calibrations simultaneously as the radiation contours from surface temperature variations are recorded.

This is accomplished as the camera views the test surface from behind, as shown in Fig. 2. In general, all ten thermocouple junction locations are present in the infrared field viewed by the camera. The exact spatial locations and pixel locations of these thermocouple junctions and the coordinates of the field of view are known from calibration maps obtained before measurements. During this procedure, the camera is focused and rigidly mounted and oriented relative to the test surface in the same way as when radiation contours are recorded. Voltages from the thermocouples are acquired using the apparatus mentioned earlier. With these data, grayscale values at pixel locations within digital images from the infrared imaging camera are readily converted to local Nusselt number values. Because such calibration data depend strongly on camera adjustment, the same brightness, contrast, and aperture camera settings are used to obtain the experimental data. The in situ calibration approach rigorously and accurately accounts for these variations.

Images from the infrared camera are recorded as enriched jpeg files, which contain information on surface temperature based on the camera's internal calibration. These images are imported to the desktop computer using ThermaCAM QuickView software provided by FLIR Systems, Inc. This same program is then used to convert the images to grayscale bit maps. These images are then imported into MATLAB® software to convert each of 256 possible grayscale values to a local Nusselt number at each pixel location using calibration data. Each individual image covers a 256 pixel by 256 pixel area.

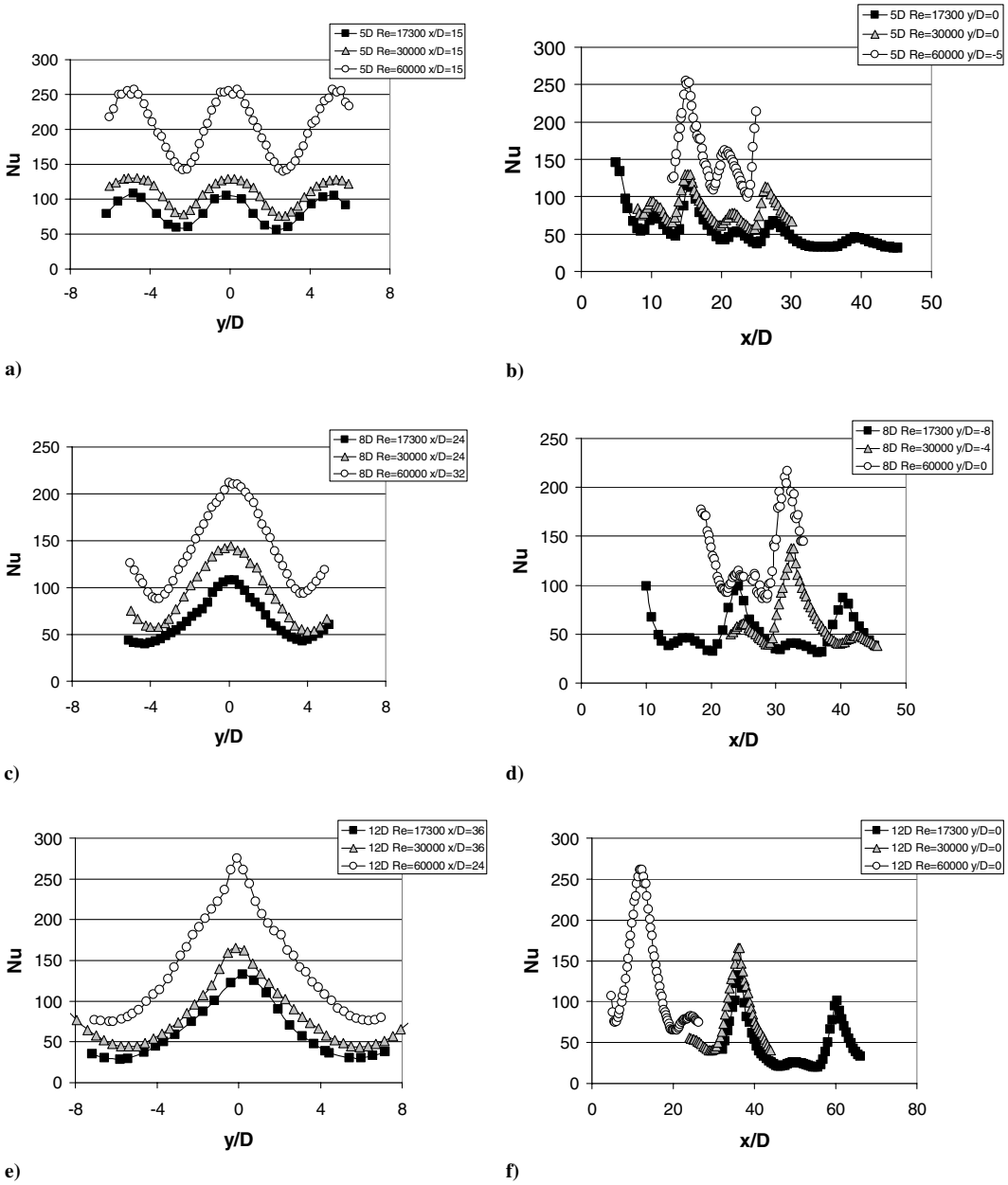

Fig. 6 Local surface Nusselt number variations for $M_a = 0.2$ and Re_j values of 17,300, 30,000–30,500, and 60,000: a) hole spacing 5*D* spanwise variations, b) hole spacing 5*D* streamwise variations, c) hole spacing 8*D* spanwise variations, d) hole spacing 8*D* streamwise variations, e) hole spacing 12*D* spanwise variations, and f) hole spacing 12*D* streamwise variations.

E. Crossflow Mass Velocity-to-Jet Mass Velocity Ratio and Discharge Coefficient

The crossflow-to-jet mass velocity ratio Gc/Gj is given by

$$\frac{Gc}{Gj} = \frac{\text{crossflow mass velocity}}{\text{jet mass velocity}} = \frac{\rho u_{\text{crossflow}}}{\rho u_{\text{jet}}} \tag{7}$$

Discharge coefficients are determined using

$$C_D = \rho_a u_a / \rho_i u_i \tag{8}$$

The first step in determining the ideal impingement mass flux $\rho_i u_i$ is obtaining an ideal impingement Mach number M_i using

$$P_{oj}/P_a = [1 + M_i^2(k-1)/2]^{k/k-1} \tag{9}$$

Next, the impingement ideal static temperature T_i (°C) is determined using T_{oj} (°C), the ideal Mach number M_i, and the appropriate ideal gas isentropic relationship. The impingement ideal static density is given by $\rho_i = P_a/RT_i$, and the impingement ideal velocity is given by $u_i = M_i(kRT_i)^{1/2}$. Note that, in most cases, discharge coefficients are determined that are based on P_a (Pa), the spatially averaged static pressure at the exits of the impingement holes. P_a (Pa) is measured by using an OMEGA HHP-102F pressure sensor.

F. Experimental Uncertainty Estimates

Uncertainty estimates are based on 95% confidence levels and are determined using methods described by Kline and McClintock [29] and Moffat [30]. The uncertainty of temperatures measured with thermocouples is ±0.15°C. Spatial and temperature resolutions achieved with infrared imaging are about 0.1–0.2 mm and 0.4°C, respectively. This magnitude of temperature resolution is due to uncertainty in determining the exact locations of thermocouples with respect to the pixel values used for the in situ calibrations. The local Nusselt number uncertainty is then about ±4.8%. Note that uncertainties of local Nusselt numbers include the effects of very small amounts of streamwise and spanwise conduction along the test surfaces employed. The Reynolds number uncertainty is about ±2.0% for Re_j values of 17,000–20,000.

III. Experimental Results and Discussion

Table 1 gives the impingement test plate configurations. Table 2 gives the experimental conditions of the present investigation.

A. Crossflow Mass Velocity-to-Jet Mass Velocity Ratio and Discharge Coefficients

Figure 4a shows the ratio of crossflow mass velocity-to-jet mass velocity as it varies with hole row number for hole spacings of 5D, 8D, and 12D. This ratio is only as high as about 0.48 at the end of all rows of holes. Here, data from the present study show reasonably good agreement with the correlation of Florschuetz et al. [9]. Note that Gc/Gj values are lower for 12D hole spacing than for 8D hole spacing, with 5D having the highest values when compared at a particular value of x/D. Discharge coefficients represent average values for all of the impingement holes on a particular test plate and are presented in Fig. 4b. From this figure, it is apparent that discharge coefficients decrease slightly as the Reynolds number increases, provided the Mach number is 0.2, and the hole spacing is maintained constant.

B. Variations of Spatially Resolved Local Nusselt Numbers with Reynolds Number at Constant Mach Number

Surface Nusselt number distributions are presented in Fig. 5 for $Ma = 0.20$ and $Re_j = 17,300$, 30,000–30,500, and 60,000 for the three different hole spacings of 5D, 8D, and 12D. The different views of the test surface are due to different infrared camera views of the target plate as different impingement plates with different Reynolds number and Mach number are employed. This is because the impingement plates that are employed are different sizes with different sizes of hole diameters. Note that, regardless of the Reynolds number and the Mach number, the qualitative distributions of local Nusselt numbers produced by each impingement jet are similar, with good periodic repeatability in the spanwise direction for each streamwise row of impact location. Figure 5 also shows that local Nusselt number *peak values* for each hole spacing generally become

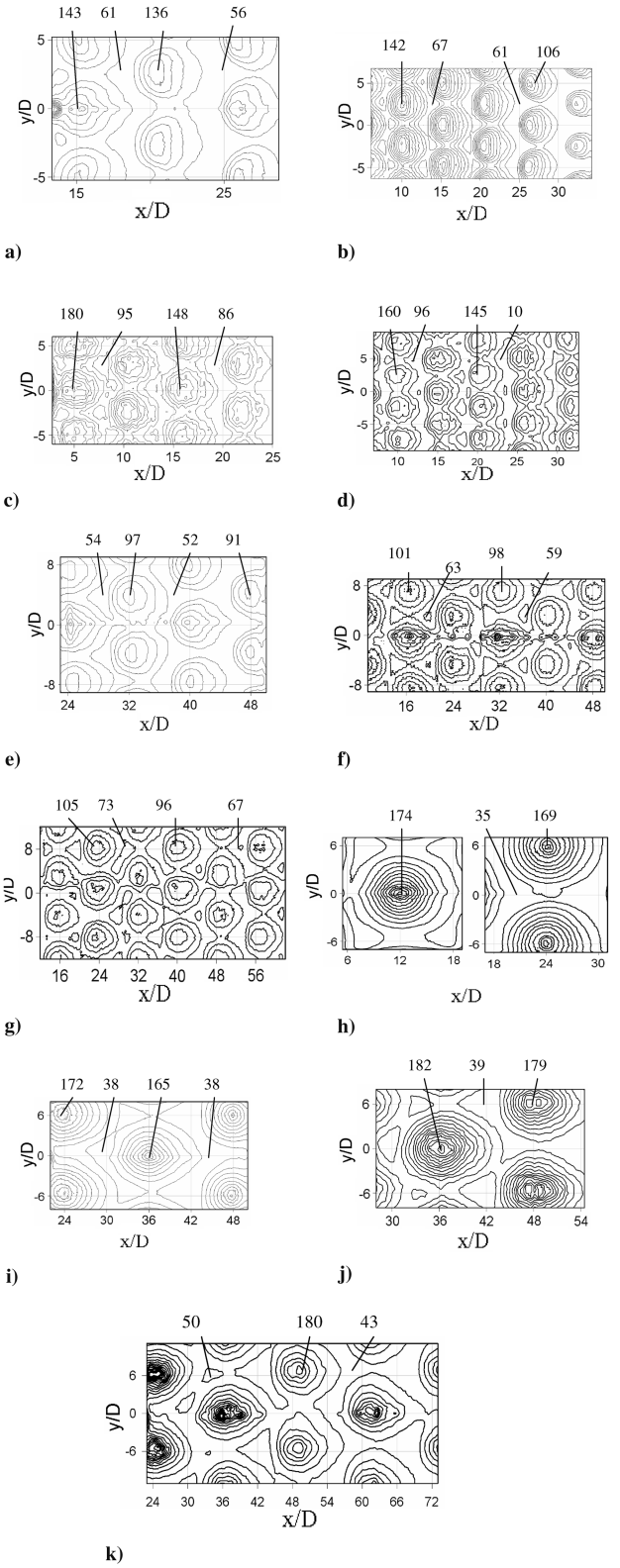

Fig. 7 Spatially resolved distributions of surface Nusselt number for $Re_j = 30,000–30,500$ with hole spacings and M_a values: a) 5D and $M_a = 0.09$, b) 5D and $M_a = 0.17$, c) 5D and $M_a = 0.30$, d) 5D and $M_a = 0.38$, e) 8D and $M_a = 0.20$, f) 8D and $M_a = 0.35$, g) 8D and $M_a = 0.45$, h) 12D and $M_a = 0.10$, i) 12D and $M_a = 0.17$, j) 12D and $M_a = 0.38$, and k) 12D and $M_a = 0.45$.

smaller at successive x/D locations for each value of impingement jet Reynolds number and Mach number due to the detrimental effect spent air crossflow has on heat transfer. The local Nusselt number decreases with x/D for $8D$ hole spacing are generally more pronounced at most all x/D locations compared to the $12D$ hole spacing data, with the decrease even more pronounced for the $5D$ hole spacing cases. This is a result of the cumulative effects of the interactions between adjacent jets and the resulting crossflows for an arrangement in which the jets are more closely spaced together.

Figures 6a–6f show local Nusselt number data for different hole Reynolds numbers at constant Mach number for each of the hole spacings, at constant values of x/D and y/D. These comparisons each show a marked increase in Nussult number values with increasing Reynolds number, for which higher values are present beneath the impingement jets and lower values are then present between jet impact locations. The constant x/D plots show symmetric periodicity in the spanwise direction, whereas the constant y/D plots show a successive decrease in periodically varying Nusselt numbers with increasing x/D due to the effects of spent air crossflow. As such, these data provide additional detail on the local Nusselt number variations given in Figs. 5a–5i. Note that somewhat different x/D ranges are occasionally present for the different data sets because different sizes of impingement plates with different impingement hole diameters are employed to achieve different test conditions (as either the Reynolds number is varied with constant Mach number, or as the Mach number is varied with constant Reynolds number).

C. Variations of Spatially Resolved Local Nusselt Numbers with Mach Number at Constant Reynolds Number

Figures 7a–7k present surface Nusselt number distributions for a constant Reynolds number of $Re_j = 30,000$–$30,500$ with Mach numbers of 0.09, 0.17, 0.30, and 0.38 for hole spacing $5D$; Mach numbers of 0.20, 0.35, and 0.45 for hole spacing $8D$; and Mach numbers of 0.10, 0.17, 0.38, and 0.45 for hole spacing $12D$. Figures 8a–8f then provide comparison plots of local data at constant x/D and y/D for each of the data sets presented in Fig. 7. For each of the three hole spacings, there is good repeatability in the spanwise direction for every experimental condition, with a decrease in local Nusselt number values with increasing x/D. This decrease with x/D is greatest for the hole spacing $5D$ and almost unnoticeable for the hole spacing $12D$, illustrating the effects of increasing amounts of

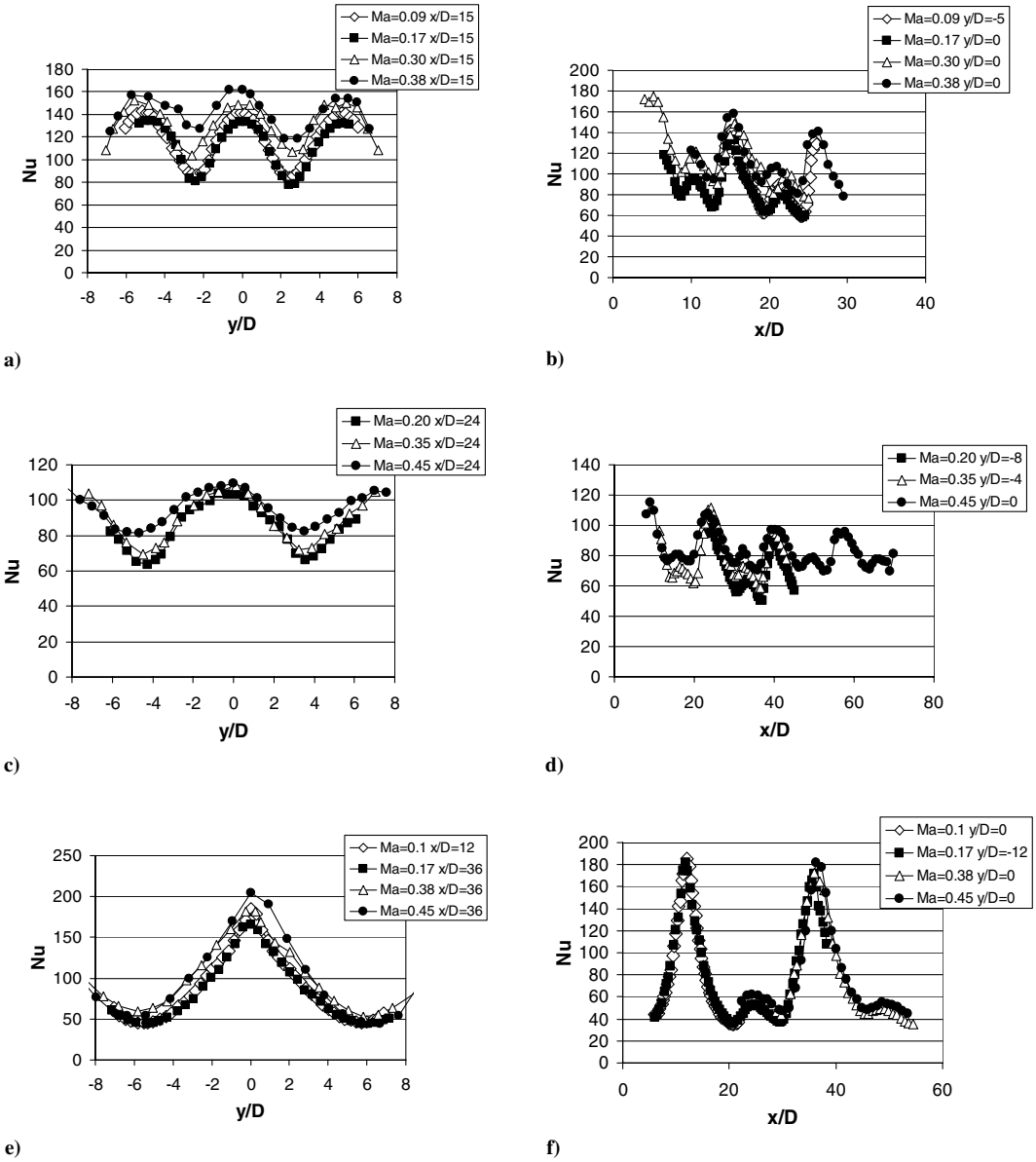

Fig. 8 Local surface Nusselt number variations for $Re_j = 30,000$–$30,500$ and M_a values of 0.1, 0.2, 0.35, and 0.45: a) hole spacing $5D$ spanwise variations, b) hole spacing $5D$ streamwise variations, c) hole spacing $8D$ spanwise variations, d) hole spacing $8D$ streamwise variations, e) hole spacing $12D$ spanwise variations, and f) hole spacing $12D$ streamwise variations.

spent air crossflow with decreasing hole spacing. Also important are increases of local Nusselt number values with increasing Mach number for each of the three hole spacings. These increases are especially apparent near local Nusselt number peak locations in Figs. 8a–8f, and are due, in part, to the effects of compressibility on the vortices and associated vortex structures that form around each impingement jet.

D. Line-Averaged Nusselt Numbers

Figures 9a–9c and 10a–10c present Nusselt numbers that are line-averaged over y/D from -2.5 to $+2.5$ for a hole spacing of $5D$, over -4.0 to $+4.0$ for a hole spacing of $8D$, and over -6.0 to $+6.0$ for a hole spacing of $12D$. Figures 9a–9c show line-averaged comparisons as the Reynolds number changes at constant Mach number for each of the three hole spacings. These Nusselt number data for each of the three hole spacings show considerable increases with Reynolds number, as well as values that decrease in a periodic fashion with streamwise development as x/D increases. This decrease with x/D is more pronounced for smaller hole spacings due to increased effects of spent air crossflow. Similar trends are evident in Figs. 10a–10c, which show line-averaged Nusselt number comparisons as the Mach number varies at constant Reynolds number for each of the three hole spacings. Here, comparisons at constant x/D and constant Reynolds number generally show increases of line-averaged Nusselt numbers with Mach number.

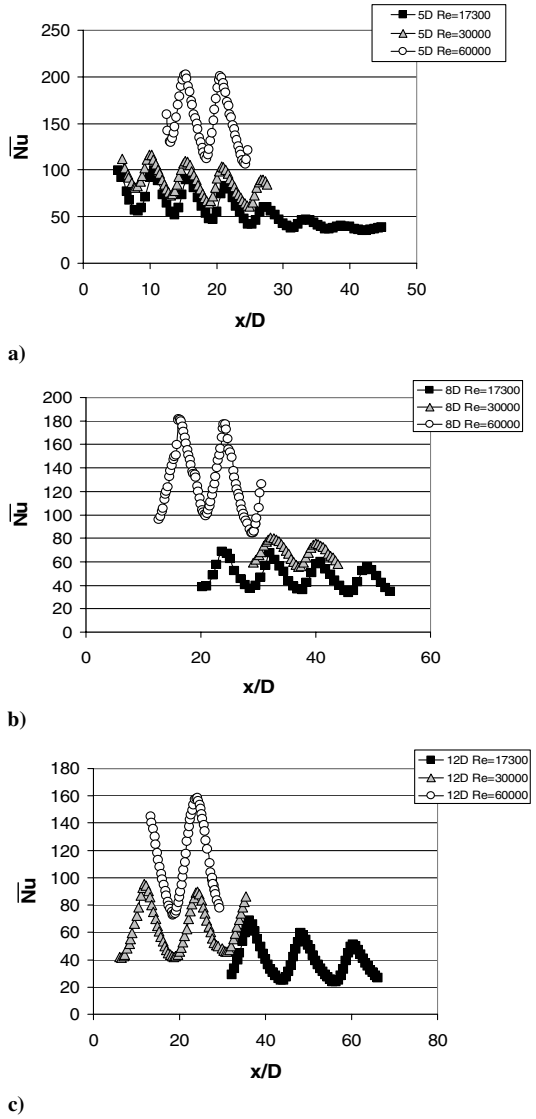

Fig. 9 Surface Nusselt number variations line-averaged over y/D for one hole spacing in either direction from the origin for a constant Mach number M_a of 0.20: a) hole spacing $5D$ and $Re_j = 17,300$, 30,500, and 60,000; b) hole spacing $8D$ and $Re_j = 17,300$, 30,500, and 60,000; and c) hole spacing $12D$ and $Re_j = 17,300$, 30,000, and 60,000.

E. Spatially Averaged Nusselt Numbers

Figures 11–13 compare measured spatially averaged Nusselt numbers for hole spacings of $5D$, $8D$, and $12D$ with correlation values from Florschuetz et al. [9]. These data are obtained by averaging over areas in the streamwise and spanwise directions, which are the same as the spanwise averaging distance used to obtain the line-averaged data.

Figure 11a shows comparisons for $5D$ hole spacing at a constant Mach number of 0.17 and Re_j values of 17,300, 30,500, and 59,000. Here, measured and correlation-predicted values are in agreement within 5–10% for the lower Re_j values. Figure 11b shows the comparison for $5D$ hole spacing at constant Reynolds number and Mach number values of 0.09, 0.17, 0.30, and 0.38. Here, the two data sets for $Ma \leq 0.2$ show good agreement with Florschuetz et al. [9], with a departure from the correlation that increases with increasing Mach number at each x/D value.

Figure 12a shows the comparison for $8D$ hole spacing at constant Mach number of 0.20 and Re_j values of 11,100, 13,100, 17,300, 30,500, and 59,000. In all cases, there is good agreement between measured and correlation-predicted values [9]. Figure 12b shows the comparison for $8D$ hole spacing at constant Reynolds number, and Mach number values of 0.10, 0.20, 0.35, 0.45, and 0.59. Here,

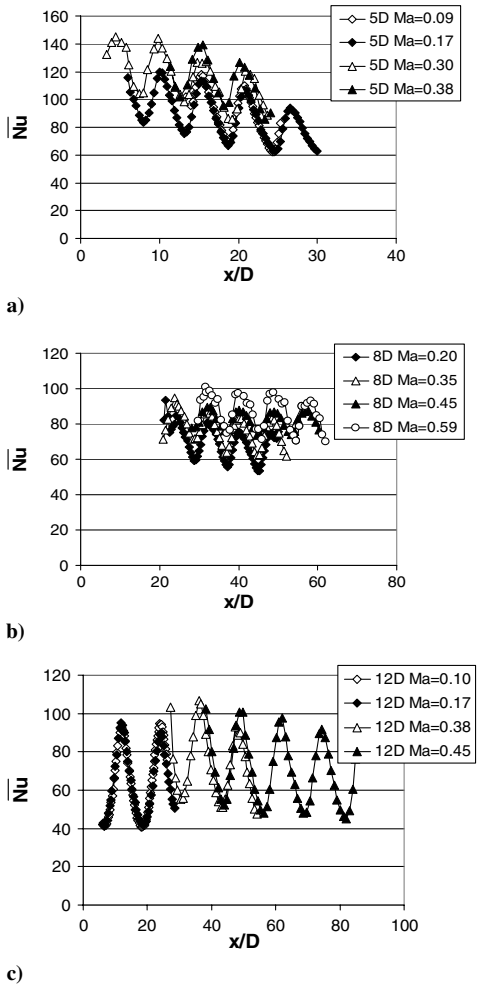

Fig. 10 Surface Nusselt number variations that are line-averaged over y/D for one hole spacing in either direction from the origin for a constant Reynolds number of 30,000–30,500: a) hole spacing $5D$ and $M_a = 0.09$, 0.17, 0.30, and 0.38; b) hole spacing $8D$ and $M_a = 0.20$, 0.35, 0.45, and 0.59; and c) hole spacing $12D$ and $M_a = 0.10$, 0.17, 0.38, and 0.45.

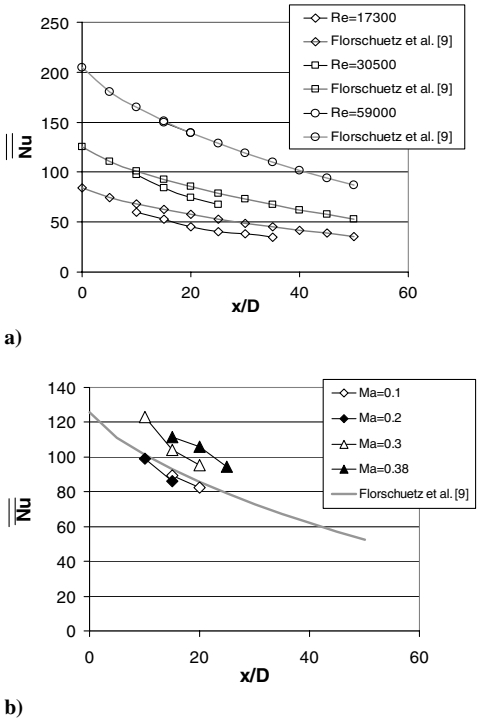

Fig. 11 Hole spacing $X/D = Y/D = 5$ comparison of area-averaged Nusselt numbers with correlation of Florschuetz et al. [9]: a) data for $M_a = 0.17$, and $Re_j = 17, 300, 30{,}500$, and $59{,}000$; and b) data for $Re_j = 30,000$ and M_a values of 0.1, 0.17, 0.30, and 0.38.

as seen for the $5D$ hole spacing data, the two cases for $Ma \leq 0.2$ show good agreement with Florschuetz et al. [9], with a departure from the correlation that increases with increasing Mach number at each x/D value.

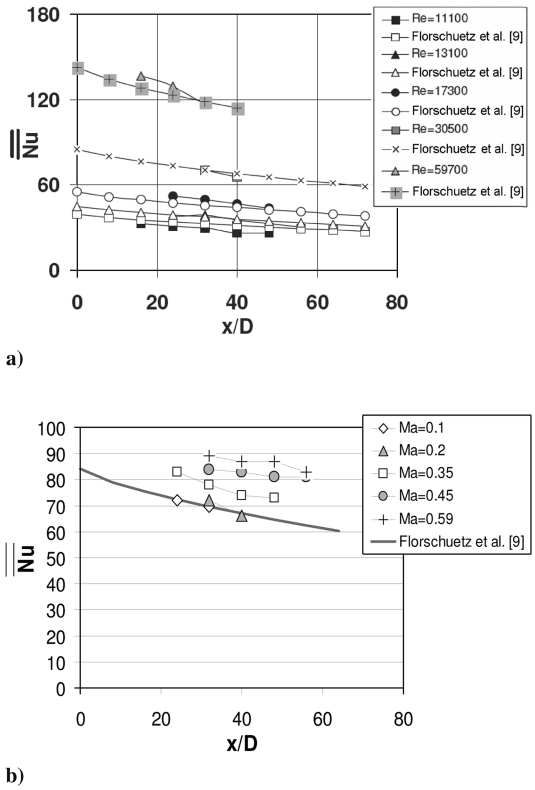

Fig. 12 Hole spacing $X/D = Y/D = 8$ comparison of area-averaged Nusselt numbers with correlation of Florschuetz et al. [9]: a) data for $M_a = 0.2$, and $Re_j = 17, 300, 30{,}500$, and $59{,}000$; and b) data for $Re_j = 30,000$ and M_a values of 0.1, 0.2, 0.35, 0.45, and 0.59.

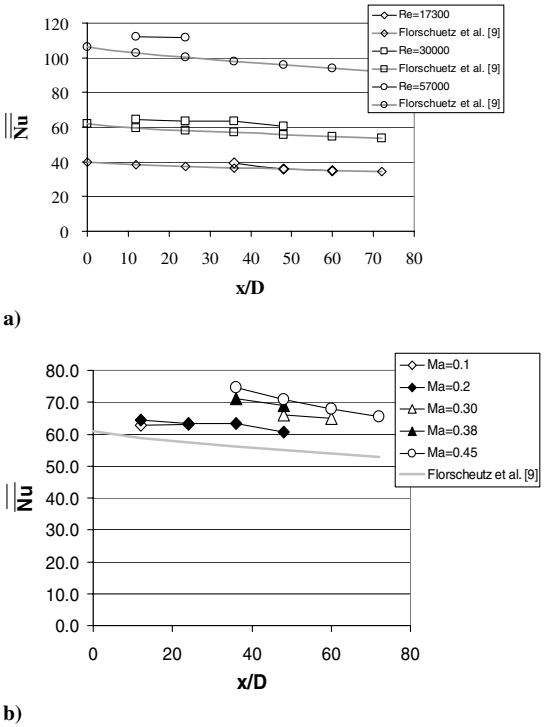

Fig. 13 Hole spacing $X/D = Y/D = 12$ comparison of area-averaged Nusselt numbers with correlation of Florschuetz et al. [9]: a) data for $M_a = 0.2$, and $Re_j = 17, 300, 30{,}000$, and $59{,}000$; and b) data for $Re_j = 30,000$ and M_a values of 0.1, 0.2, 0.35, 0.38, and 0.45.

Figure 13a shows that, at constant Mach number, the data for hole spacing $12D$ show good agreement with the correlation-predicted values for $Re_j = 17,300$. When $Re_j = 30,000$ and $57,000$, measured values are then higher than predicted values. Figure 13b shows that, for incompressible cases, when $Ma = 0.11$ and 0.22, spatially averaged Nusselt number values are in agreement with each other, but higher than the predicted values of Florschuetz et al. [9]. These differences are not surprising when one considers that the $12D$ hole spacing data are outside the range of applicability of the correlation of Florschuetz et al. [9], which does not consider geometries with hole spacing greater than $8D$ for a staggered array. Area-averaged Nusselt numbers then increase with Mach number at each x/D value in Fig. 13b, which is consistent with results presented in Figs. 11b and 12b for the two smaller hole spacings.

F. Effects of Compressibility on Area-Averaged Nusselt Numbers

The variations due to different impingement jet spacings are partially because each jet produced using the larger spacing of $X/D = Y/D = 12$ approximates the behavior of an individual jet. When $X/D = Y/D = 8$ and $X/D = Y/D = 5$, the cumulative effects of induced crossflows partially reduce the effectiveness of each individual jet. However, because the jets are closer together, with greater local influences of surrounding jets, line-averaged and area-averaged Nusselt numbers are generally higher as X/D and Y/D decrease.

Of importance to such changes are the vortices that form around the impinging jets and then interact with each other after they impact on the target surface [12]. Interactions of these jet vortices with the accumulation of crossflows from sequential rows of jets, which are especially apparent in associated data for the $5D$ and $8D$ jet spacings, are also important, and generally give general trends of decreasing local and spatially averaged Nusselt numbers with x/D. These interactions are tied to the unsteady vortex structures and vortex rings that initially form around the periphery parts of the impingement jets. According to Fox et al. [12], it is the competition between these vortex rings and the associated secondary vortices induced by them that determine the local stagnation temperature and static temperature distributions on the impingement target plate. The resulting total

temperature alterations from these vortices are then also responsible for enhancing the surface heat transfer and the surface Nusselt number distributions. Depending upon the interactions between the primary and secondary vortex rings after they impact and advect along the target plate, different amounts and distributions of surface heating and/or cooling can be produced [12].

Compressibility, even in a mild form, alters these complex vortex interactions. Complications and complexity also result as the compressible vortex rings and the associated secondary vortices from different impingement jets intermingle and interact with each other in a myriad of possible forms and combinations. The results of these interactions are evident in the data presented in Figs. 5–13, which show that the associated changes are generally most apparent in local values, than values that are line averaged or area averaged.

Existing correlations for arrays of impinging jets generally do not include compressible flow effects. To partially resolve this deficiency, spatially averaged Nusselt numbers are compared to the correlation of Florschuetz et al. [9] for $Re_j = 30,000$ and values of Mach number that range from 0.1 to 0.45 in Figs. 14a–14c. This is accomplished by presenting the dependence on impingement jet Mach number M_a, of $\overline{\overline{Nu}}/\overline{\overline{Nu}}_F$, the ratio of the area-averaged Nusselt number to the area-averaged Nusselt number at the same experimental conditions determined from the correlation of Florschuetz et al. [9]. As such, Fig. 14a shows the Mach number dependent deviation from the predicted values of Florschuetz et al. for hole spacing $X/D = Y/D = 5$, whereas Figs. 14b and 14c present this information for hole spacings of $X/D = Y/D = 8$ and $X/D = Y/D = 12$, respectively. These data are given for specific x/D values.

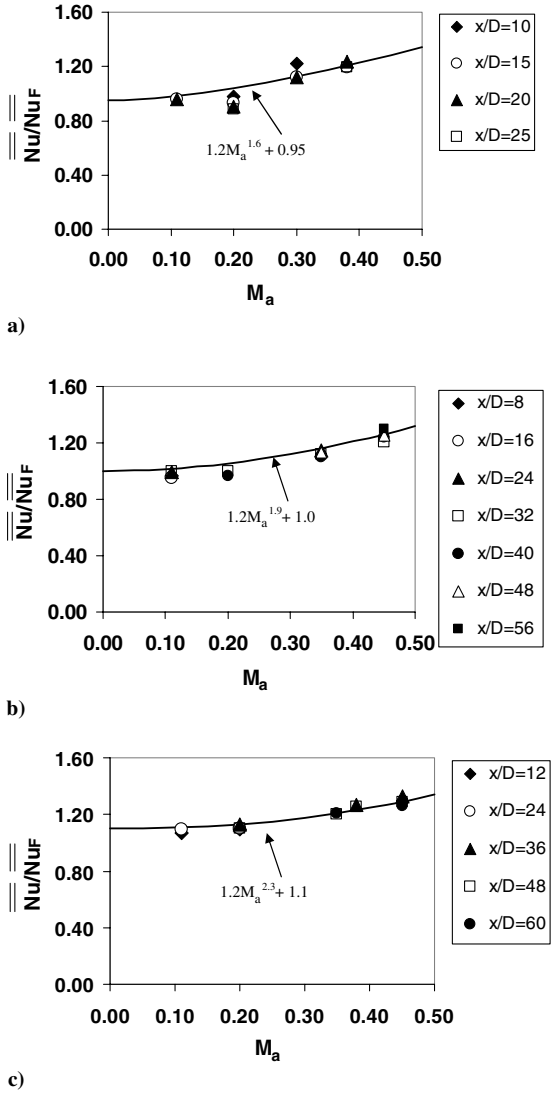

Fig. 14 Area-averaged Nusselt number variations with Mach number: a) $X/D = Y/D = 5$, $Re_j = 30,500$ and M_a values of 0.11, 0.20, 0.30, and 0.38; b) $X/D = Y/D = 8$, $Re_j = 30,500$ and M_a values of 0.11, 0.20, 0.35, and 0.45; and c) $X/D = Y/D = 12$, $Re_j = 30,000$ and M_a values of 0.11, 0.20, 0.35, 0.38, and 0.45.

For $X/D = Y/D = 5$, the correlation equation that best represents these data is given by

$$\overline{\overline{Nu}}/\overline{\overline{Nu}}_F = 0.95 + 1.2M_a^{1.6} \tag{10}$$

For $X/D = Y/D = 8$, the associated correlation equation is given by

$$\overline{\overline{Nu}}/\overline{\overline{Nu}}_F = 1.0 + 1.2M_a^{1.9} \tag{11}$$

For $X/D = Y/D = 12$, the resulting correlation equation is given by

$$\overline{\overline{Nu}}/\overline{\overline{Nu}}_F = 1.1 + 1.2M_a^{2.3} \tag{12}$$

The present data thus deviate from the correlation of Florscheutz et al. [9] by larger amounts as the impingement Mach number increases, with the largest deviation evident for $M_a = 0.59$. As such, the trends shown by the data in Figs. 14a–14c are qualitatively consistent with results from Brevet et al. [22] for a single impingement jet.

IV. Conclusions

New experimental data are provided as the jet hole spacing is varied for Reynolds numbers from 17,300 to 60,000, and for Mach numbers as high as 0.45. The spacings between the holes in the streamwise direction X are then $5D$, $8D$, or $12D$, and the spanwise spacings between the holes in a given streamwise row Y are also $5D$, $8D$, or $12D$. The thickness of each impingement plate is $1D$, and the spacing between the hole exit planes and the target plate is denoted as Z and is equal to $3D$. These data are given for an array of impinging jets in the form of ratios of crossflow mass velocity-to-jet mass velocity, discharge coefficients, spatially resolved local surface Nusselt numbers, line-averaged Nusselt numbers, and spatially averaged Nusselt numbers.

The measured Nusselt number data for each of the three hole spacing configurations show strong dependence on Mach number, for Mach numbers greater than 0.2 as Reynolds number is held constant. The correlations developed from these experimental data show that increasing the Mach number improves heat transfer for each geometry to differing degrees, with the strongest Mach number dependence for the $X/D = Y/D = 12$ array. When the impingement jet Mach number is less than about 0.2, local, line-averaged, and area-averaged data show strong Reynolds number dependence, but almost no dependence on Mach number for each jet spacing. Each jet produced using $X/D = Y/D = 12$ approximates the behavior of an individual jet, whereas the influences of surrounding jets, including the cumulative induced crossflows and interactions of jet-induced vortex structures, become more pronounced when $X/D = Y/D = 8$ and when $X/D = Y/D = 5$. The present experimental data also show that spatially averaged Nusselt numbers are generally higher for smaller hole spacings than for more sparse arrays when compared at the same streamwise location. In addition, the $12D$ jet spacing area-averaged Nusselt number data show the least variation with x/D, whereas the $5D$ jet spacing shows the largest. Corresponding periodic line-averaged Nusselt number data show that values decrease significantly at successive x/D locations for $X/D = Y/D = 5$, whereas data for $X/D = Y/D = 12$ are approximately invariant with x/D.

Regardless of the Reynolds number and the Mach number, the qualitative local Nusselt number distributions produced by different impingement jets are similar, with good periodic repeatability in the spanwise direction for each row of streamwise impact location. Crossflow mass velocity-to-jet mass velocity ratio data are lower for sparse arrays than for dense arrays when compared at a particular value of x/D, with reasonably good agreement with the correlation of Florschuetz et al. [9].

Acknowledgment

The research that led to the results presented in this paper was sponsored by Solar Turbines, Inc., located in San Diego, California.

References

[1] Martin, H., "Heat and Mass Transfer Between Impinging Gas Jets and Solid Surfaces," *Advances in Heat Transfer*, Vol. 13, Academic Press, New York, 1977, pp. 1–60.

[2] Schulz, A., "Combustor Liner Cooling Technology in Scope of Reduced Pollutant Formation and Rising Thermal Efficiencies," *Heat Transfer in Gas Turbine Systems*, Vol. 934, 2001, pp. 135–146.

[3] Kercher, D. M., and Tabakoff, W., "Heat Transfer by a Square Array of Round Air Jets Impinging Perpendicular to a Flat Surface Including the Effect of Spent Air," *Transactions of the ASME. Journal of Engineering for Power*, Vol. 92, 1970, pp. 73–82.

[4] Metzger, D. E., Yamashita, T., and Jenkins, C., "Impingement Cooling of Concave Surfaces with Lines of Circular Air Jets," *Transactions of the ASME. Journal of Engineering for Power*, Vol. 91, 1971, pp. 149–158.

[5] Chupp, R., Helms, H., McFadden, P., and Brown, T., "Evaluation of Internal Heat-Transfer Coefficients for Impingement Cooled Turbine Airfoils," *Journal of Aircraft*, Vol. 6, No. 3, 1969, pp. 203–208. doi:10.2514/3.44036

[6] Metzger, D. E., and Korstad, R., "Effects of Crossflow on Impingement Heat Transfer," *Transactions of the ASME. Journal of Engineering for Power*, Vol. 94, 1972, pp. 35–41.

[7] Chance, J. L., "Experimental Investigation of Air Impingement Heat Transfer Under an Array of Round Jets," *TAPPI 57*, Vol. 6, 1974, pp. 108–112.

[8] Metzger, D. E., Florschuetz, L. W., Takeuchi, D. I., Behee, R. D., and Berry, R. A., "Heat Transfer Characteristics for Inline and Staggered Arrays of Circular Jets with Crossflow of Spent Air," *Journal of Heat Transfer*, Vol. 101, 1979, pp. 526–531.

[9] Florschuetz, L. W., Truman, C. R., and Metzger, D. E., "Streamwise Flow and Heat Transfer Distributions for Jet Array Impingement with Crossflow," *Journal of Heat Transfer*, Vol. 103, 1981, pp. 337–342.

[10] Obot, N. T., and Trabold, T. A., "Impingement Heat Transfer Within Arrays of Circular Jets: Part 1—Effects of Minimum, Intermediate, and Complete Crossflow for Small and Large Spacings," *Journal of Heat Transfer*, Vol. 109, 1987, pp. 872–879.

[11] Bunker, R., and Metzger, D. E., "Local Heat Transfer in Internally Cooled Turbine Airfoil Leading Edge Regions: Part 1—Impingement Cooling Without Film Extraction," *Journal of Turbomachinery*, Vol. 112, 1990, pp. 451–458. doi:10.1115/1.2927680

[12] Fox, M. D., Kurosaka, M., Hedges, L., and Hirano, K., "The Influence of Vortical Structures on the Thermal Fields of Jets," *Journal of Fluid Mechanics*, Vol. 255, 1993, pp. 447–472. doi:10.1017/S0022112093002551

[13] Bailey, J. C., and Bunker, R. S., "Local Heat Transfer and Flow Distributions for Impinging Jet Arrays of Dense and Sparse Extent," American Society of Mechanical Engineers Paper GT-2002-30473, June 2002.

[14] Taslim, M. E., Pan, Y., and Bakhtari, K., "Experimental Racetrack Shaped Jet Impingement on a Roughened Leading-Edge wall With Film Holes," American Society of Mechanical Engineers Paper GT-2002-30477, June 2002.

[15] Li, X., Gaddis, J. L., and Wang, T., "Mist/Stream Heat Transfer with Jet Impingement onto a Concave Surface," American Society of Mechanical Engineers Paper GT-2002-30475, June 2002.

[16] Parsons, J. A., Han, J. C., and Lee, C. P., "Rotation Effect on Jet-Impingement Heat Transfer in Smooth Rectangular Channels with Four Heated Walls and Radial Crossflow," *Journal of Turbomachinery*, Vol. 120, 1996, pp. 79–85.

[17] Parsons, J. A., Han, J. C., and Lee, C. P., "Rotation Effect on Jet-Impingement Heat Transfer in Smooth Rectangular Channels with Four Heated Walls and Coolant Extraction," American Society of Mechanical Engineers Paper GT-2003-38905, June 2003.

[18] Parsons, J. A., and Han, J. C., "Rotation Effect on Jet Impingement Heat Transfer in Smooth Rectangular Channels With Coolant Extraction," *International Journal of Rotating Machinery*, Vol. 7, 2001, pp. 87–103.

[19] Epstein, A. H., Kerrebrock, J. L., Koo, J. J., and Preiser, U. Z., "Rotational Effects on Impingement Cooling," *Symposium on Transport Phenomena in Rotating Machinery*, 1985.

[20] Mattern, C., and Hennecke, D. K., "Influence of Rotation on Impingement Cooling," American Society of Mechanical Engineers Paper GT-1996-161, May 1996.

[21] Brevet, P., Dejeu, C., Dorignac, E., Jolly, M., and Vullierme, J. J., "Heat Transfer to a Row of Impinging Jets in Consideration of Optimization," *International Journal of Heat and Mass Transfer*, Vol. 45, 2002, pp. 4191–4200. doi:10.1016/S0017-9310(02)00128-X

[22] Brevet, P., Dorignac, E., and Vullierme, J. J., "Mach Number Effect on Jet Impingement Heat Transfer," *Heat Transfer in Gas Turbine Systems*, Vol. 934, 2001, pp. 409–416.

[23] Behbahani, A. I., and Goldstein, R. J., "Local Heat Transfer to Staggered Arrays of Impinging Circular Air Jets," *Transactions of the ASME. Journal of Engineering for Power*, Vol. 105, 1983, pp. 354–360. doi:10.1115/1.3227423

[24] San, J.-Y., and Lai, M.-D., "Optimum Jet-to-Jet Spacing of Heat Transfer for Staggered Arrays of Impinging Air Jets," *International Journal of Heat and Mass Transfer*, Vol. 44, 2001, pp. 3997–4007. doi:10.1016/S0017-9310(01)00043-6

[25] Downs, S. J., and James, E. H., "Jet Impingement Heat Transfer—A Literature Survey," American Society of Mechanical Engineers Paper 87-HT-35, Nov. 1987.

[26] Jambunathan, K., Lai, E., Moss, M. A., and Button, B. L., "A Review of Heat Transfer Data For Single Circular Jet Impingement," *International Journal of Heat and Fluid Flow*, Vol. 13, No. 2, 1992, pp. 106–115. doi:10.1016/0142-727X(92)90017-4

[27] Viskanta, R., "Heat Transfer to Impinging Isothermal Gas and Flame Jets," *Experimental Thermal and Fluid Science*, Vol. 6, 1993, pp. 111–134. doi:10.1016/0894-1777(93)90022-B

[28] Goodro, M., Park, J., Ligrani, P. M., Fox, M., and Moon, H.-K., "Effect of Hole Spacing on Spatially-Resolved Jet Array Impingement Heat Transfer," *International Journal of Heat and Mass Transfer*, Vol. 51, Nos. 25-26, 2008, pp. 6243–6253. doi:10.1016/j.ijheatmasstransfer.2008.05.004

[29] Kline, S. J., and McClintock, F. A., "Describing Uncertainties in Single Sample Experiments," *Mechanical Engineering*, Vol. 75, 1953, pp. 3–8.

[30] Moffat, R. J., "Describing the Uncertainties in Experimental Results," *Experimental Thermal and Fluid Science*, Vol. 1, No. 1, 1988, pp. 3–17. doi:10.1016/0894-1777(88)90043-X